Integrating Materials and Manufacturing Innovation (2018) 7:202–213
https://doi.org/10.1007/s40192-018-0122-y

TECHNICAL ARTICLE

Numerical Prediction of the Microstructure and Stress Evolution During Surface Grinding of AISI 52100 (DIN 100Cr6)

Ali Rajaei[1] · Bengt Hallstedt[1] · Christoph Broeckmann[1] · Sebastian Barth[2] · Daniel Trauth[2] · Thomas Bergs[2]

Received: 13 September 2018 / Accepted: 21 November 2018 / Published online: 17 December 2018

Abstract
Grinding is one of the most important finishing processes in industrial production. During grinding, the workpiece is subjected to thermomechanical loads. Thermal damage can occur in terms of microstructure changes due to a critical temperature history. A holistic model of the relevant physical load fields and their interactions would help describe and predict the influence of grinding loads on the residual stresses in the surface zone of the workpiece. In this paper, a very promising approach is introduced to simulate grinding of the hardened and tempered bearing steel AISI 52100 using the Finite Element Method (FEM). A material model was developed to describe the thermomechanical and metallurgical changes of the bearing steel under the process loads. Material properties were modeled depending on the temperature and microstructure changes. Temperature gradients, microstructure evolution, thermal, and phase transformation strains were integrated in the model to predict the residual stress state after grinding. Experimental and simulative investigations were conducted for pendulum grinding, and the measured and simulated residuals stresses were compared. The depth of the subsurface zone, where thermally influenced microstructural changes occur, varied with changes of the process parameters. Experiments and simulations showed compressive stresses in the re-hardened zone and tensile stresses in the tempered area.

Keywords Grinding · Residual stresses · Finite element method · Phase transformation · Grind hardening

Introduction

Grinding is the final step in the production of many hardened components. By grinding, a high surface quality and a high material removal rate can be attained at the same time. The process generates a combined thermomechanical load, which affects the surface integrity in terms of residual stresses in the surface zone. It can cause changes in the microstructure and hardness of the workpiece and can lead to cracks and undesired microstructure [1]. The grinding heat can trigger phase transformations in the surface zone. Above certain temperatures, a hardenable steel is austenitized and then re-hardened by martensitic, and conceivably bainitic, transformation due to high cooling rates under coolant flow. Until today, only a few finite element (FE) studies have dealt with phase transformations during grinding and their effects on the residual stresses in the workpiece surface zone [2–4]. The effects of thermal loads, mechanical loads, and phase transformations on residual stresses were first combined by Zhang and Mahdi [5–7]. The transformation of austenite to martensite was also explicitly defined in their models, but the volume change associated with the phase transformations, which has a significant effect on the residual stress evaluation, was not taken into account. Further investigations were carried out by Brinksmeier et al. [8] in which the phase transformation of AISI 52100 steel (DIN 100Cr6) during the grind hardening process and the heat affected zone were simulated using thermo-metallurgical-coupled analyses. However, the residual stresses in the surface layer after grind hardening were not calculated. Salonitis and Chryssolouris [9] conducted a similar study with the focus on the temperature distribution in the workpiece during grinding, considering temperature dependent thermal properties. The heat flux into the surface layer was modeled by a simplified triangular profile. To evaluate the

✉ Ali Rajaei
a.rajaei@iwm.rwth-aachen.de

[1] Institute of Applied Powder Metallurgy and Ceramics (IAPK) at RWTH Aachen University e.V, Augustinerbach 4, 52062 Aachen, Germany

[2] Laboratory for Machine Tools and Production Engineering (WZL), RWTH Aachen University, Campus-Boulevard 30, 52074 Aachen, Germany

hardness in the depth of the surface zone after grinding, the temperature within the workpiece was compared with the austenitization temperature. Moreover, the increase of the austenitization temperature due to the rapid heating was considered. However, none of those approaches considered the influence of phase transformations on the residual stresses during grinding of an already hardened and tempered workpiece. The main goal of the present work is the comprehensive analysis of stress evolution mechanisms in hardened and tempered steel during grinding, using the FEM. This required experimental investigations of grinding forces and temperatures, grinding wheel contact length, and the real kinematic total grain contact surface. In addition, the material behavior was investigated, aiming to observe the arising metallurgical changes and to obtain material properties and model parameters for a quantitative description of the material response.

Material and Experimental Methods

To assure a reproducible process and material test results, all samples were machined under the same process conditions and from the same material batch of AISI 52100 bearing steel. The analyzed chemical composition is given in Table 1. The samples were already heat treated before grinding by austenizing at 850 °C for 30 min, quenching to room temperature, and tempering at 220 °C for 120 min, leading to a hardness of 60 ± 1 HRC. An average-retained austenite fraction of about 7% was determined by X-ray diffraction after tempering. All grinding samples were cuboids of the same size, $L = 80$ mm; $W = 20$ mm; $H = 15$ mm.

In Situ Grinding Force and Temperature Measurements

Experimental tests were carried out on a surface grinding machine Blohm Profimat MT 408 to analyze the thermal and mechanical loads alongside the contact zone. According to the process limits of the machine, the table speed v_w and the circumferential speed of the grinding wheel v_s were varied. In addition, the specific material removal rate Q'_w was varied, by changing the depth of cut a_e. The grinding experiments were repeated two times.

A detailed analysis of the correlation between process parameters and the surface load exposure of the samples could only be ascertainable based on the knowledge of the grinding forces and temperatures in the contact zone. Therefore, a measurement system was developed that allowed the in-situ determination of the process forces and temperatures locally along the contact arc and the total force upon the sample. So far, research activities have focused mainly on the description of the total grinding force, which is the sum of the single force components in the tangential direction F_t and in the normal direction F_n applied on the real kinematic contact surface between the grinding wheel grains and the sample. The developed force-measuring platform in this work enabled the recording of the tangential and normal grinding forces $F_{t,arc}$ and $F_{n,arc}$ along the contact arc with a high temporal and spatial resolution. Figure 1 shows a schematic representation of the platform (Fig. 1b) and exemplary measuring results (Fig. 1a). The total grinding force components were constant during the grinding process, until the grinding wheel passed the red marked force-measuring adapter (Fig. 1b). The adapter recorded the force differential and enabled the analysis of the grinding force as a function of the position in the contact arc, while the total grinding force was measured below by a Kistler dynamometer.

Besides force measurement, the grinding wheel topography was analyzed to determine the kinematic contact area between grinding wheel and sample. This was done in order to determine the effective pressure on the contact surface. The topography was recorded by optical evaluation of negative imprints of the grinding wheel surface. Afterwards, the measured grinding wheel surfaces were analyzed with a MATLAB-based software called Topo-tool, which was programed to identify the kinematic engagement surfaces and to calculate the kinematic contact area, depending on the process parameters [10]. Consequently, the maximum surface pressure $p_{n,max}$ on the sample could be calculated as a measure of the mechanical load on the sample surface zone in the normal direction.

The simultaneous determination of the thermal and mechanical loads during the grinding process was realized with the temperature measuring method used by Duscha [11]. A constantan-resistance alloy foil (55% Cu, 44% Ni, and 1% Mn) was connected to a constantan wire with an OMEGA TL-WELD-220 V thermocouple-welding unit. The resulting metal conductor was fixed between two screwed sample-halves. Ceramic mica discs were used to isolate the constantan foil from the sample. Simultaneously, the downstream sample-half was connected to a reference junction using an Fe-conductor. During the grinding process, the constantan foil is machined and plastically deformed, so that a contact to the downstream sample-half is closed across the ceramic isolation. The closed contact between the metal pair enabled the temperature measurement based on the thermoelectric voltage. Figure 2 shows the microscope pictures of the constantan foil before (a) and after (b) passing of the grinding wheel as well as scanning electron microscopic (SEM) pictures of the constantan foil after the passing the grinding wheel (c)–(d) to clarify the plastic deformation.

Table 1 The analyzed chemical composition of AISI 52100

C	Si	Mn	P	S	Cr	Mo	Ni
0.932	0.219	0.371	0.0053	0.0103	1.41	0.0219	0.0583

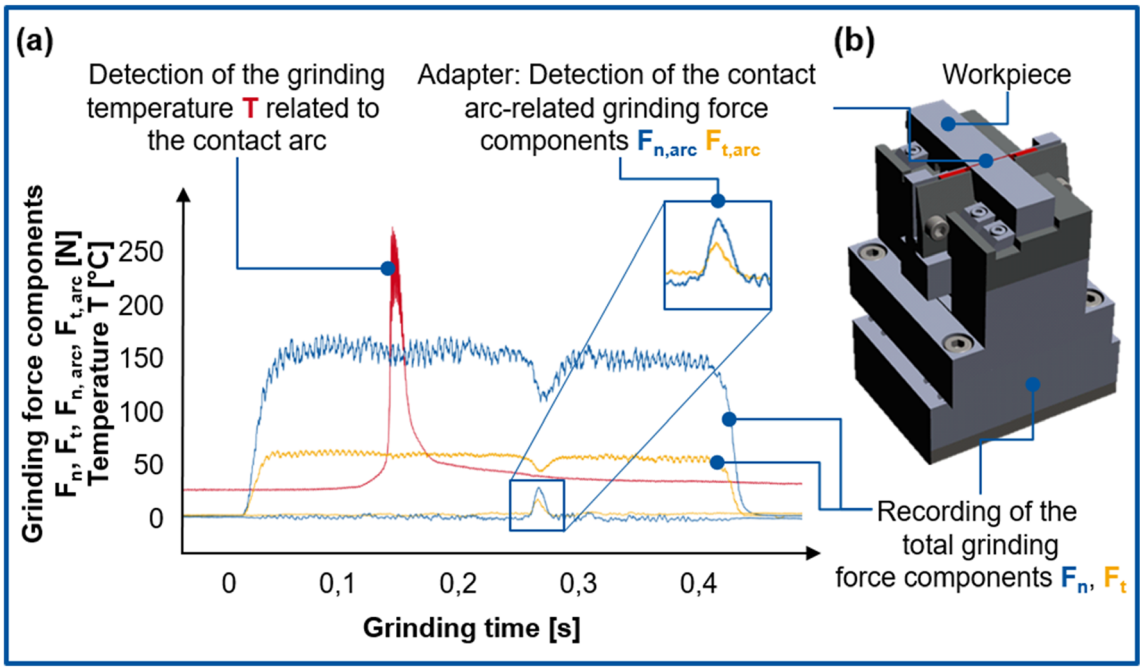

Fig. 1 A schematic representation of the platform (**b**) and exemplary measuring results (**a**).

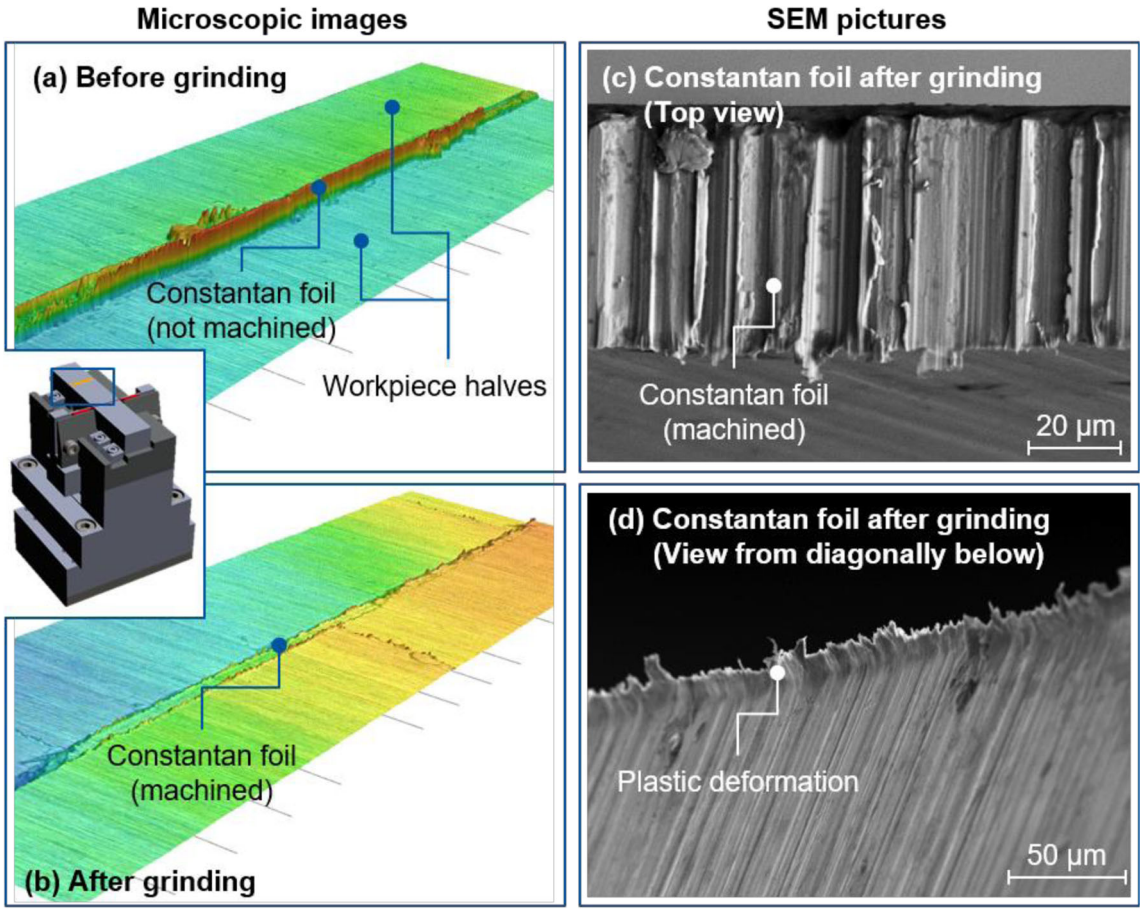

Fig. 2 Microscopic pictures of the constantan foil before (**a**) and after (**b**) passing of the grinding wheel as well as scanning electron microscopic (SEM) pictures of the constantan foil after the passing the grinding wheel (**c**–**d**) to clarify the plastic deformation

Dilatometric Tests

During grinding, the surface zone of the workpiece undergoes an indirect heat treatment cycle. Extreme high heating and cooling rates can result in a short time austenitization ($\alpha \rightarrow \gamma$ transformation) during heating and formation of a new hardening zone by the transformation of austenite to martensite by rapid cooling. Besides ($\alpha \leftrightarrow \gamma$)-phase transformations, precipitation can also be associated with volume change and induce local transformation strains. By increasing the temperature, martensite gradually loses its tetragonal structure and turns into cubic martensite.

Dilatometric tests were conducted on AISI 52100 cylindrical samples, $D = 4$ mm and $L = 10$ mm, in a TA Instruments DIL 805A/D/T quenching dilatometer to investigate the transformation kinetics under different thermal conditions. Figure 3 shows length changes in two stages before austenitization. These are regarded as the precipitation of transition iron carbides with the composition of $Fe_{2.4}C$, known as ε-carbides, and cementite Fe_3C, respectively. Tempered martensite (as the initial microstructure) does not show the first stage during heating because the transition carbides are already formed during tempering. The transformation of retained austenite (RA) in AISI 52100 is observed during heating and usually in the temperature range of 230–300 °C, parallel to cementite precipitation [12]. However, the exact kinetics of this transformation is hard to monitor by means of dilatometry because the volume increase caused by RA-transformation is overlapped by the volume decrease during cementite precipitation.

Metallography

The surface zone of the workpiece is subjected to quasi-heat treatment and mechanical stress during grinding. Both have an influence on the internal stresses during cooling and the resulting residual stress state in the surface zone. Thus, the distribution of residual stresses in the surface zone of the workpieces was measured. For this purpose, residual stress analyses in three directions was determined by X-ray diffraction on the specimens. Due to the limited penetration depth of X-rays to only a few µm of the surface, the workpiece surface was gradually removed between the individual measurements by means of electrochemical polishing. The lattice strain measurements were carried out with a mobile X-ray diffractometer from Stresstech (XSTRESS3000, goniometer type G2R) arranged according to the $\sin^2\Psi$ method (see Fig. 4). Doing so, the lattice plane distances were determined from the position of the diffraction lines at different measurement angles.

The line position was determined at the interference recorded with two location-sensitive semiconductor detectors, taking into account the Lorentz and polarization factors. The line position was determined using the cross correlation method including the $K\alpha$-separation.

The determined line positions (grid plane distances) resulted in a linear course over the measuring angle $\sin^2\Psi$ if no significant changes of the normal stress components σ_{ii} occurred within the penetration depth, and no pronounced texture and no significant plastic deformations were present. The gradients of the distributions were determined by linear regression described the by lattice strains. The stresses were calculated according to Hooke's law using the X-ray elasticity constants $-s_1$ and $½s_2$, which take into account the anisotropy of the material when measuring the respective lattice planes.

Modeling Physical Interactions During Grinding

The evolution of the internal stresses during grinding is the outcome of excessive thermomechanical process loads. Depending on the process parameters, the grinding force (mechanical load) or the process heat (thermal load) can be the dominant cause for residual stresses. The temperature change due to high friction values in grinding might trigger phase

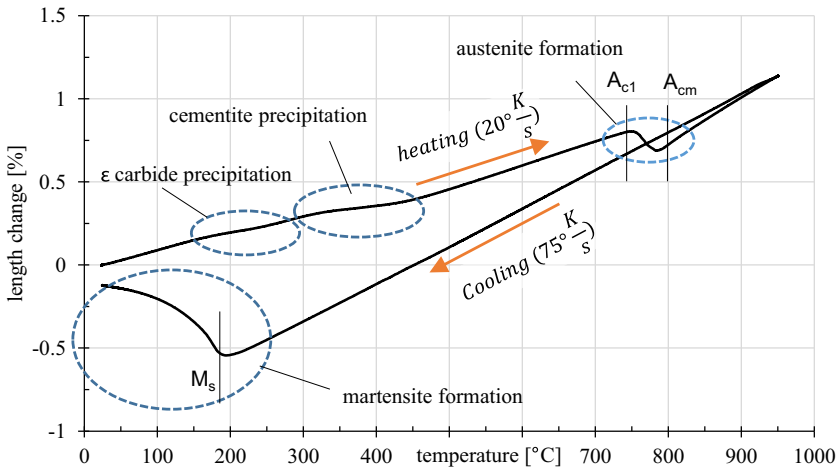

Fig. 3 Length changes in two stages before austenitization

a)

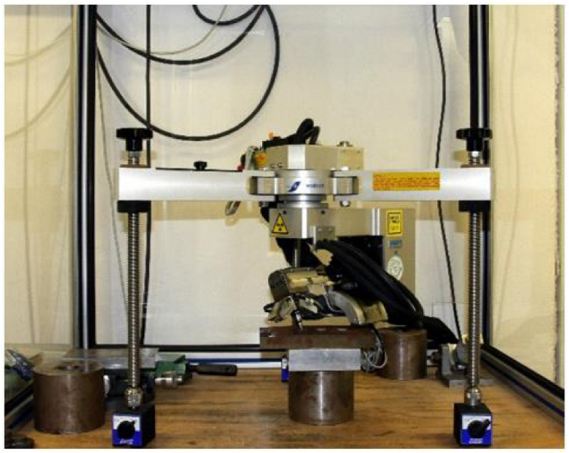

b)

Radiation/ Filter / High Voltage	Cr-K_α / Vanadium / 30 kV
Lattice array {hkl}	{211}
Diffraction angles 2Θ	156.2°
Measuring direction	0°; 45°; 90°
Measuring angle range Ψ	± 45°
Number of tipping angles	13
Measurement place	Ø 3.0 mm
Mean penetration depth of X-rays	4.7 µm

Fig. 4 Mobile X-ray diffractometer from Stresstech (XSTRESS3000, goniometer type G2R) (**a**) and measurements (**b**)

transformations in the surface zone, which significantly influence the stress evolution. Hence, there exists a multi-physics process with coupling interactions between the physical fields, as shown schematically in Fig. 5 [11, 13, 14].

The kinetics of the phase transformation depend generally on the temperature and temperature rates. However, prior plastic strains and the stress state also affect the transformation kinetics. During phase transformations, the heat of the transformation can change the thermal state slightly. Furthermore, phase transformations can induce strains. The transformation-induced strain is partially due to the volume mismatch between the parent and new phases, and partially due to transformation plasticity (TRIP) [15]. Besides the indicated field interactions, the microstructure/temperature dependency of the material properties should be noticed.

Temperature Distribution

The temperature distribution in the workpiece depends on the thermal boundary conditions, the thermal properties of the material, and the transformation heat. The transformation of phase i to phase k leads to a change of enthalpy $\Delta H_{i\rightarrow k}$. The rate of heat generation by the transformation is determined by Eq. (1). $\dot{q}_{\mathrm{tr}}$ is the rate of the transformation heat, $\dot{p}_k$ is the transformation rate and ρ_k is the density.

$$\dot{q}_{\mathrm{tr}} = \Delta H_{i\rightarrow k} \cdot \dot{p}_k \cdot \rho_k \tag{1}$$

The definition of the boundary condition includes the process heat flow to the surface zone of the workpiecec during the grinding process and the subsequent heat transfer by the coolant. The setup of the boundary conditions is explained in the section "Simulation Model" and "Results and Discussion".

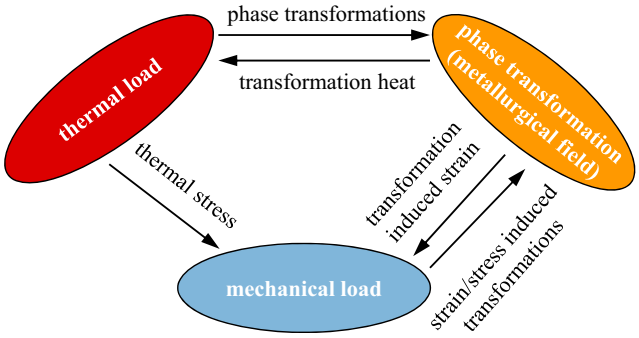

Fig. 5 Multi-physics process with coupling interactions between the physical fields

Phase Transformation

To describe the diffusion-controlled transformations quantitatively, usually the Johnson-Mehl-Avrami (JMA) model is used [16–17]. There are several modifications to the JMA-model and different methods for determination of the model parameters in the literature [18–20]. Available modifications take into account the effect of temperature rates, plastic strains, and stresses on the transformation kinetics. In this work, the suggested model by Li et al. [20] was adopted. The evolution of the new "phase" is given under the assumption that the nucleation rate is equal to zero, i.e., all nuclei are formed at $t = 0$, and the transformation rate is controlled only by the growth rate. The JMA model is simplified as follows:

$$p = 1 - \exp\left(-gN_0\left[\frac{k_0}{\beta}\int_{T0}^{T}\exp\left(\frac{Q}{\mathrm{RT}(t)}\right)\mathrm{dt}\right]^n\right) \tag{2}$$

$$p = 1 - \exp(-\eta^n) \tag{3}$$

with:

$$\eta = \frac{K}{\beta}\int_{T0}^{T}\exp\left(-\frac{Q}{\mathrm{RT}}\right)\cdot \mathrm{dT}$$

$$K = gN_0k_0$$

In Eq. (2), p is the fraction of the new phase, g is a geometrical growth factor, N_0 is the number of pre-existing nuclei, k_0 is an exponential factor depending on the material and the type of transformation, β is the heating rate, T is the temperature, Q is the activation energy of the transformation, R is the gas constant, t is the time, and n is the Avrami-exponent. The advantage of this approach is that the model parameters Q, K, and n can be determined directly from the dilatometric curves without regression analysis.

Cooling rates under application of the coolant during grinding are often high enough to transform austenite into martensite, if the surface zone is austenitized. The Koistinen-Marburger [21] model describes the martensite fraction p_m as a function of temperature T (4):

$$p_m = p_{\max} \cdot \left(1 - \exp\left(-\frac{(M_s - T)}{b}\right)\right) \tag{4}$$

The variable $p_{\max}$ is the maximum possible martensite fraction, constant b is determined to be 70 °C by dilatometric tests and M_s is the start temperature of the martensitic transformation. The M_s temperature depends on the austenite stability, which is mainly influenced by the chemical composition. During short time austenitization, cementite might dissolve only partially in austenite and therefore, the carbon content of austenite depends on the maximum temperature reached in the surface zone and the austenitization time. In the simulation model, M_s is defined as a function of the maximum temperature, based on dilatometric tests.

Strain/Stress State

The thermomechanical-metallurgical interactions discussed earlier lead to a time and location dependent total strain ε_{ij}^{t} in the material. A very common assumption for small strains is that the total strain is given by a linear additivity principle as follows [13, 19, 22]:

$$\varepsilon_{ij}^{t} = \varepsilon_{ij}^{el} + \varepsilon_{ij}^{pl} + \varepsilon_{ij}^{th} + \varepsilon_{ij}^{tr} + \varepsilon_{ij}^{tp} \tag{5}$$

It is assumed that the elastic ε_{ij}^{el}, plastic ε_{ij}^{pl}, thermal ε_{ij}^{th}, transformation ε_{ij}^{tr} strains, and the transformation plasticity ε_{ij}^{tp} are independent and relatively small.

The elastic strain is calculated by the Abaqus solver based on Hooke's law and given elastic parameters. To determine the plastic strain, the von Mises criterion is considered for yielding. The flow stress of AISI 52100 is experimentally investigated in this work, and an empirical model is adopted to describe the plastic behavior, i.e., the work hardening. The flow stress is defined by the power law model according to Eq. (6). An empirical rule of mixture was adopted from [19, 23] to approximate the yield stress of the homogenized microstructure, Eq. (7).

$$\sigma_f^{(\varphi)} = \sigma_y^{(\varphi)} + k \cdot \varepsilon_{\mathrm{pl}}^{n} \tag{6}$$

$$\sigma_F = f(P_\alpha) \cdot \sigma_f^{(\alpha)} + (1 - f(P_\alpha)) \cdot \sigma_f^{(\gamma)} \tag{7}$$

$\sigma_f^{(\varphi)}$ and $\sigma_y^{(\varphi)}$ are the flow stress of the phase φ with and without hardening, k and n are hardening parameters, σ_F is the flow stress of the phase mixture, $f(P_\alpha)$ is a weighting factor adopted from [19], and P_α is the sum of ferritic (bcc) phases.

The thermal and transformation strains as well as the TRIP-effect are modeled based on dilatometric experiments. The density of the dilatometer samples was measured before the test as a reference value $\rho(T_0)$. The temperature-dependent density during heating/cooling and phase transformations is given in relation with the phase specific thermal expansion, which is the slope of the dilatometric curve, Eq. (8).

$$\rho(T) = \rho(T_0) \cdot \exp\left(-\int_{T_0}^{T} 3 \cdot \alpha(T)\, \mathrm{dT}\right) \tag{8}$$

Equation (9) describes the relationship between thermal strain, transformation strain, and density change [24, 25].

$$\varepsilon^{\mathrm{th}} + \varepsilon^{\mathrm{tr}} = \sqrt[3]{\frac{\rho(T_0)}{\rho(T)}} - 1 \tag{9}$$

During phase transformations, an additional plasticity is given due to internal or external stresses, while the equivalent applied stress is lower than the yield stress of both initial and final phases. This effect is called transformation plasticity and obviously cannot be described by von Mises criterion. The model of Fisher et al., Eq. (10) was adopted to describe the TRIP effect [15, 19].

$$\varepsilon_{ij}^{tp} = \frac{3}{2} K S_{ij} \cdot (1 - \ln(p)) \cdot p \tag{10}$$

K is a constant, S_{ij} is the deviatoric tensor and p is the transformed phase fraction.

Simulation Model

The thermomechanical load collective along the contact zone was determined experimentally for different process parameters. Depending on the process parameters (table speed v_w, depth of cut a_e, etc.), thermomechanical stresses and maybe even phase transformations arise in the surface zone within a certain depth. During grinding, material is removed and thus, only a part of the originally affected zone remains, where residual stresses can be measured. It should be noted, that the present model considers only the effective thermomechanical load collective applied to the remaining

surface zone, where the residual stresses are measured after the grinding process. The actual chip removal process is not considered. Therefore, a pre-analysis was conducted to obtain the effective loads on the ground surface. In a thermal analysis, the measured temperature profile was applied to the contact arc as a boundary condition. The temperature distribution as well as the effective heat flux into the workpiece were calculated. The thermal simulation was divided into several steps. In each step, a new contact arc was defined representing the current position of the grinding wheel. The effective pressure was simulated in a subsequent thermomechanical analysis, having the temperature distribution from the thermal analysis and by applying the measured pressure profile on the contact surface. Next, the calculated effective heat flux and the pressure profiles were applied as moving loads to the model, and the grinding process was simulated to predict the microstructure evolution and residual stresses by a coupled thermomechanical and metallurgical analysis. Figure 6 illustrates the approach to determine the effective load collective for the simulation of grinding.

To simulate the grinding process, a 3D-model was built in Abaqus, containing 65,664 linear tetrahedral elements of type C3D8RT. The minimum element size of 10 µm was given in the middle of the grinding surface within ~ 80 µm in depth. The meshing was generated in a way that elements get larger towards the model sides and bottom to reach a maximum edge length of 500 µm. Thermal and mechanical boundary conditions (BC) were assigned to the side surfaces and the bottom surface as illustrated in Fig. 7. The effective thermomechanical load collective was modeled in user subroutines DFLUX and DLOAD as moving heat flux and pressure profiles with the feed speed v_w. Using xy-symmetrical BC, the model size, and thus simulation time, was reduced. The described model was used to simulate the residual stresses with different process parameters, i.e., feed speeds v_w and depths of cut a_e. The effective load collective was obtained in each case as explained in the previous section (Fig. 6). The thermophysical properties of AISI 52100 steel were adopted from [26].

Results and Discussion

The distribution of residual stresses was the main quantity to be evaluated by comparing the simulation results with experiment. To understand the stress evolution in the workpiece during grinding, thermomechanical and metallurgical effects are analyzed in the following.

Extremely high heating and cooling rates in the surface zone result in temperature gradients, which induce thermal stresses. The material yields plastically due to the thermal stresses and the pressure of the grinding wheel. Depending on the process parameters, the effect of mechanical or thermal loads could dominate. The grinding heat dissipates into the workpiece and affects the material. The depth of the thermally affected zone depends on the effective heat flux into the workpiece, table speed v_w and the thermal conductivity of the workpiece material. Under high heating rates, cementite precipitation from martensite and austenitization are shifted to higher temperatures (above 350 °C and 760 °C, respectively) [11, 20, 27]. By exceeding transformation temperatures, new tempered and new hardened zones appear in the cross section.

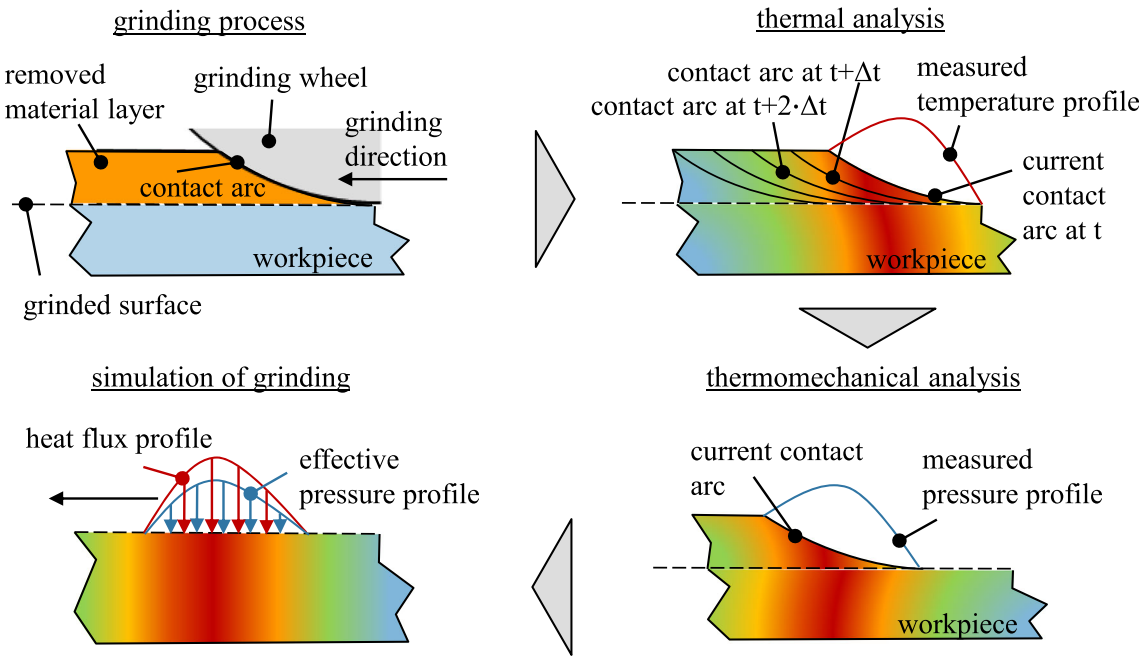

Fig. 6 The approach to determine the effective load collective for the simulation of grinding

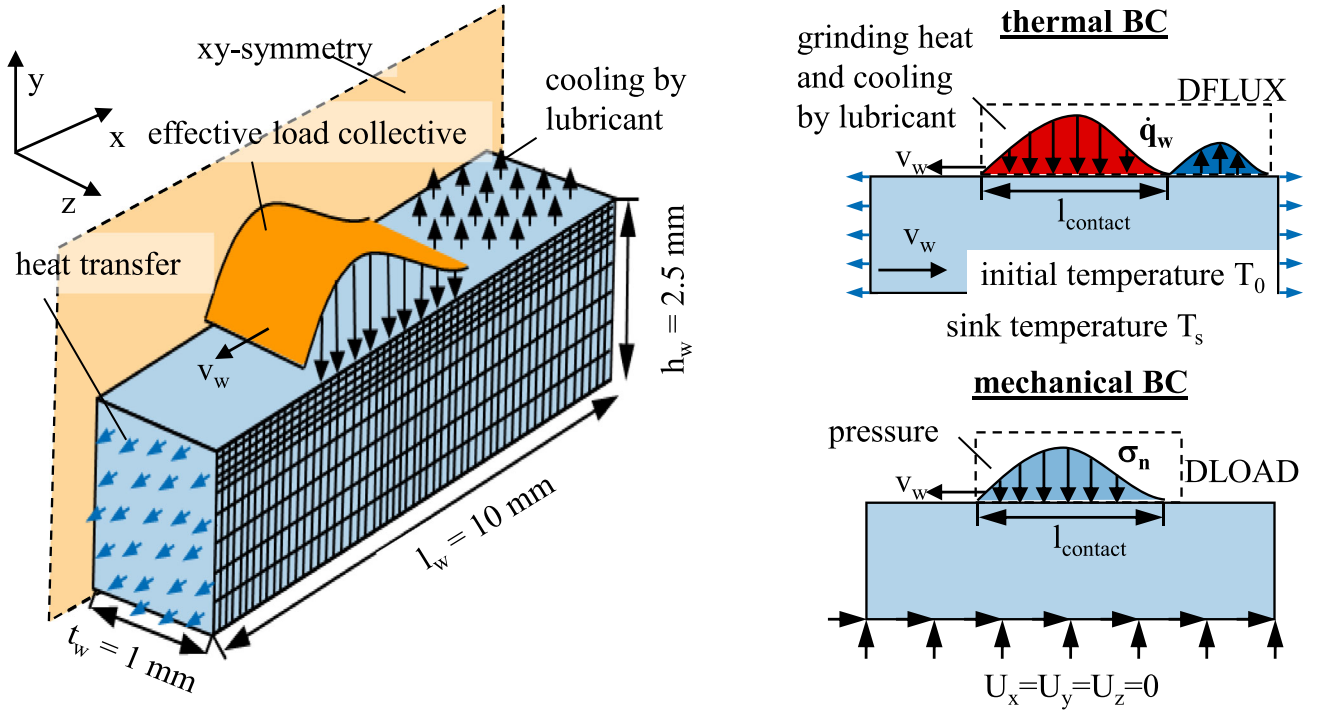

Fig. 7 Thermal and mechanical boundary conditions (BC)

Figure 8 shows the simulated microstructure after grinding with a feed speed of $v_w = 12$ m/min and the depth of cut $a_e = 0.2$ mm, compared to the experiment. The microstructure near to the surface, up to 40 µm, appears as a white area by etching, indicating a new hardening zone. The dark area given in a depth of about 40–300 µm is the tempering zone, where cementite precipitates. In the new hardening zone, material is austenitized during heating and martensite hardened subsequently during cooling. In the tempering zone, material is tempered further. The maximum temperature in the tempering zone remains below the austenitization temperature. The material seems to be thermally unaffected from a depth of ~300 µm towards the bottom. The diagram in Fig. 8 compares the simulated maximum temperature with the volume fraction of the fresh martensite after grind hardening and the further tempered martensite after cementite precipitation along the depth. Martensite volume fraction indicates an austenitization depth of about 70 µm. However, a volume fraction of more than 50% martensite is given only within 40 µm.

Cementite precipitation, austenitization, and martensitic transformation are associated with a volume change, Fig. 3. In case of such local microstructural changes, transformation strains induce local stresses. A complicated multi-axial stress state develops due to the superposition of thermal stresses, mechanical stresses, and transformation stresses. Depending on the deviatoric stress components, further directional plasticity is given due to the TRIP-effect, Eq. (10). Figure 9 compares the simulated thermal and transformation strains in x- and z-directions. The strain curves indicate that the cementite precipitation is followed by austenitization and martensitic transformation in the new hardening zone. The kinetics of the cementite precipitation in the tempering zone is different from the new hardening zone due to different local heating rates. The vital effect of the transformation plasticity becomes more obvious by comparing the simulated strain curves with ($\varepsilon^{th+tr+tp}$) and without (ε^{th+tr}) considering the TRIP-effect. Both thermal and transformation behavior of the material are assumed isotropic; however, the strain curves in x- and z-directions slightly diverge as the phase transformations are triggered. The directionality of the strain curve results from the stress dependent transformation plasticity and the deviatoric stress tensor S_{ij}, considering that $S_{xx} \neq S_{zz}$. In this work, the transformation plasticity is modeled by an explicit integration scheme, which means that the changes of the stress state due to transformation plasticity during an increment are not coupled with the calculation of the transformation plasticity. Therefore, the time increments during phase transformations must be small enough to avoid non-physical sharp and drastic changes in the stress/strain state.

Finally, the simulated and measured residual stresses after grinding are compared in Fig. 10 for different feed speeds v_w and depths of cut a_e. Stresses were measured by X-ray diffraction method (XRD). The average X-ray-penetration depth of about 4–5 µm implied that material had to be removed stepwise for further XRD-measurements. The material removal was carried out by electro-chemical polishing to minimize thermomechanical interactions within the sample, which

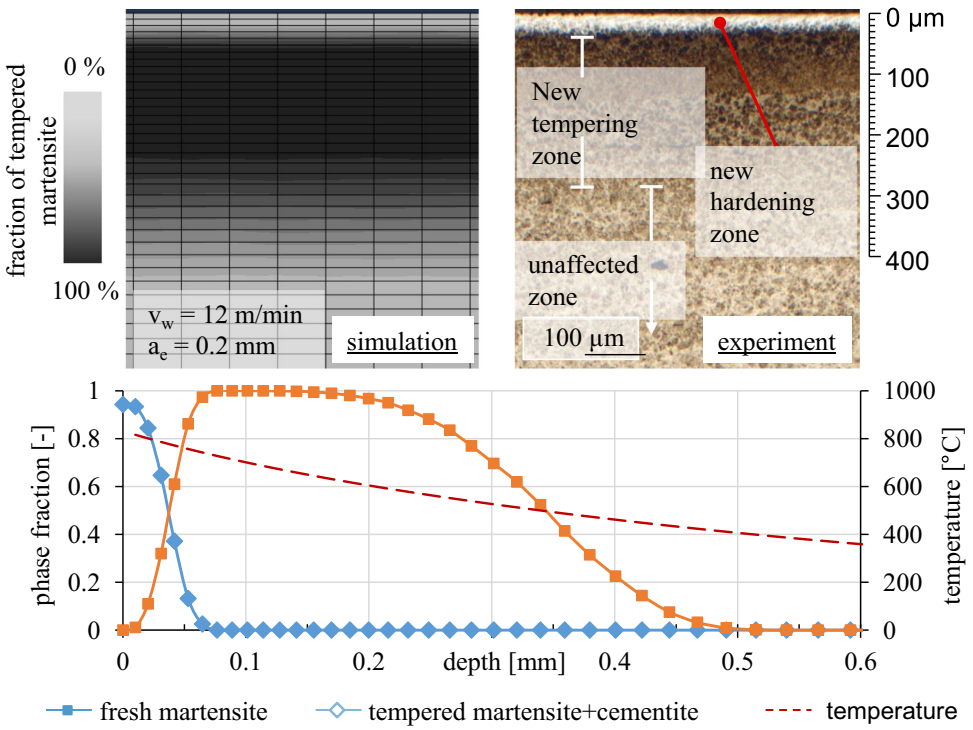

Fig. 8 A diagram that compares the simulated maximum temperature with the volume fraction of the fresh martensite after grind hardening and the tempered martensite after cementite precipitation along the depth

could influence the residual stress state [11]. The stresses were measured in longitudinal (σ_{xx}) and transversal (σ_{zz}) directions. All samples exhibit compressive stresses in the surface layer, which corresponds to the depth of the new hardening zone. The local formation of martensite in the surface layer is known as the dominating cause of the compressive stresses [11, 13, 28]. In the tempering zone, tensile stresses reach a plateau and decrease towards the unaffected zone. Figure 10 compares the simulated and measured residual stresses in the longitudinal and transversal directions after grinding with different process parameters. The simulation results are in good quantitative agreement with the measured stress distributions, indicating

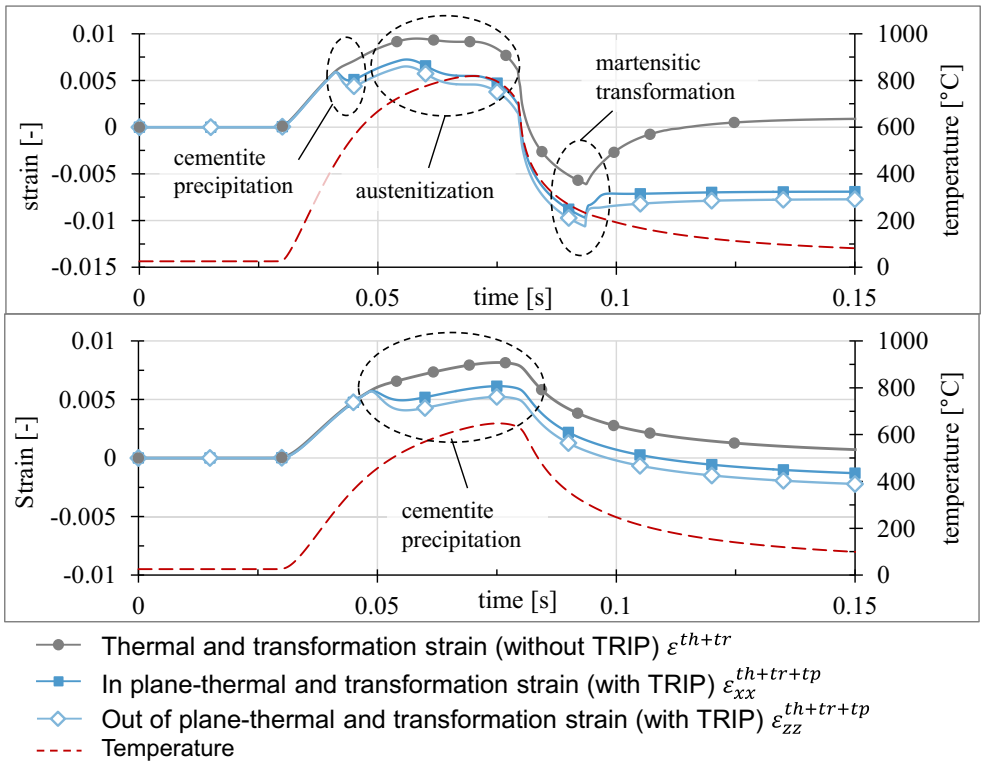

Fig. 9 A comparison of the simulated thermal and transformation strains in x- and z-directions

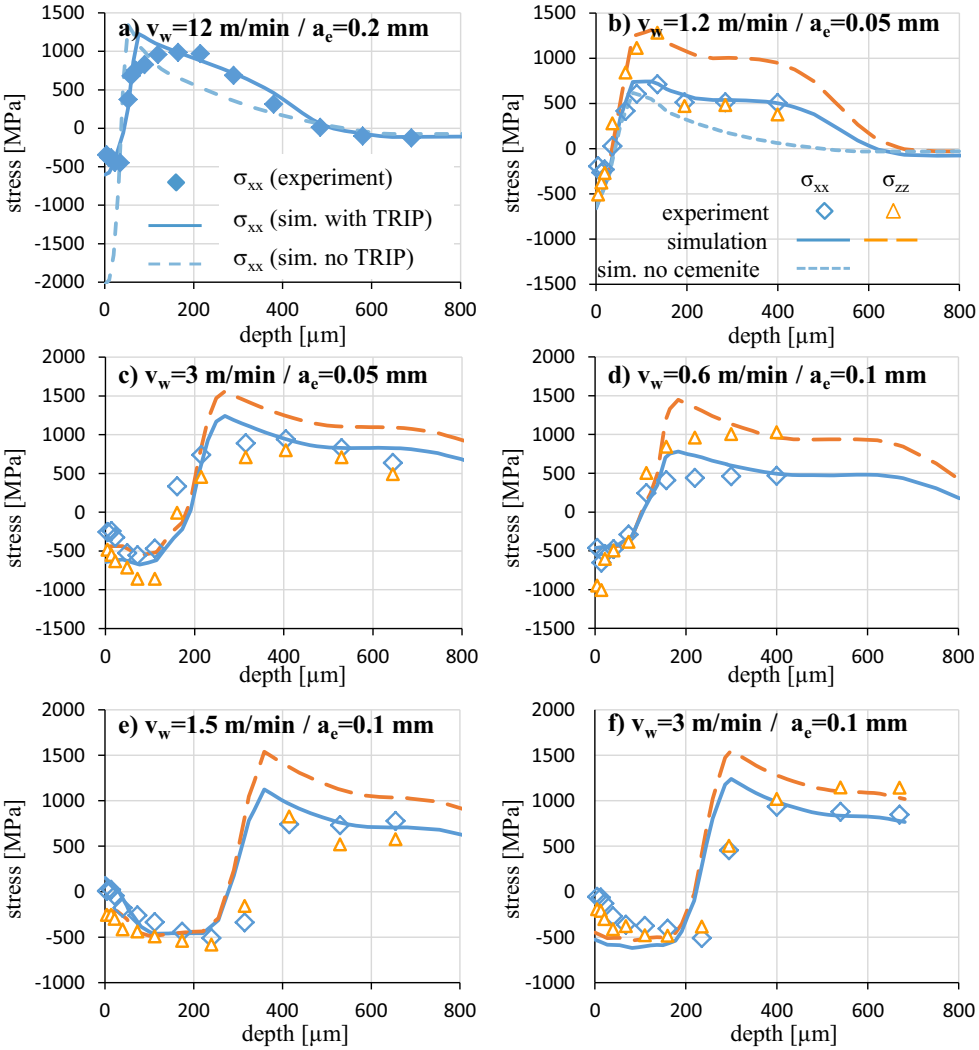

Fig. 10 Comparison of the simulated and measured residual stresses in the longitudinal and transversal directions after grinding with different process parameters

that the model covers the essential effects and interactions properly. For instance, Fig. 10(a) and (b) shows that the measured stress distribution could not be predicted without considering the transformation plasticity and cementite precipitation. The deviations of the simulated stresses from the measurements are due to the simplifications in the modeling of the grinding process, besides the uncertainties of the stress measurements. The model does not cover material removal. During the real process, the abrasive material removal generates radial and tangential forces along the contact arc. Very high local plastic deformations, under high deformation rate, are given near the grinding surface, which is not considered in the model. This could explain the deviation of the simulated compressive residual stresses from experiments in the vicinity of the surface [11]. Furthermore, XRD-tests on three samples before grinding have shown average residual stresses of $\overline{\sigma}_{xx} = -330 \pm 60$ MPa and $\overline{\sigma}_{zz} = -545 \pm 25$ MPa on the surface. The manufacturing history and the corresponding initial residual stresses of the samples were not considered in the simulations. The impact of the material removal, deformation, and initial residual stresses on the final stress state depend on the process parameters. Hence, a systematic deviation of the simulated residual stresses from measurements is hard to observe.

The model is capable of predicting residual stresses after grinding with different process parameters. For a good agreement of the predicted stresses with the measurements, the description of the effective thermomechanical loads must be as close as possible to the reality. The heat flux profile on the surface and the table speed are the boundary conditions with the highest impact on the simulation results, determining whether and how deep microstructural changes are triggered in the surface zone. Of course, thermal properties have to be defined accurately as well to calculate the transient temperature distribution in the workpiece. Thermal and mechanical properties are defined as functions of temperature and phase fractions. Therefore, the thermomechanical material response depends on the microstructure changes. Due to the finding by material investigations, cementite precipitation was identified as a very important event besides austenitization and

subsequent hardening. All phase transformations are associated with property and volume change and cause TRIP under stresses. The significant contribution of the phase transformations to the stress evolution must be considered in the modeling, which requires a description of the transformation kinetics under extreme high heating rates and short austenitization time during grinding. For the multi-phased microstructure, homogenized material properties must be determined. The overall yield/flow stress of the microstructure is modeled by a simple homogenization scheme with weighting factors for austenite and martensite. Covering all the mentioned effects, the comprehensive model can be utilized as a predictive tool to support the establishment of process guidelines to avoid excessive damage by correlating the microstructure changes and stress evolutions to the process parameters.

Conclusions

A novel approach was developed to model the grinding process and the material's thermomechanical and metallurgical response in the ground sample depending on the process loads. It is able to predict the microstructure and residual stresses on a continuum level. Experimental results showed the impact of the grinding strategy on the material's response in terms of the residual stresses. Compressive and tensile residual stresses form in the new hardening zone and new tempering zone, respectively. The depth of the thermally damaged zone depends on the process parameters and the resulting heat flux into the workpiece. As temperature increases, cementite precipitate at 230–300 °C, and the carbon content of martensite is lowered, resulting in a density change and volume decrease. If the austenitization temperature is exceeded, a new hardening zone appears after the grinding due to the rapid cooling by the coolant. The new hardening and tempering zones appear as white and dark areas under microscope. Besides the transformation strain due to the density change, the transformation plasticity showed a significant impact on the calculated residual stresses. The quantitative prediction of the residual stresses after grinding requires a comprehensive material model that covers the relevant physical interactions such as phase transformations and precipitations as well as transformation strain and transformation plasticity.

Future Work

For a better description, both process and material models need to be improved. The approximation of the effective heat flux can be enhanced by measuring the temperature in the sample depth during grinding. The presented simulation results correspond to the last grinding stroke for each process and the initial residual stress state is neglected. Further potential future work could be the modeling of the heat treatment prior to the grinding process as well as the modeling of subsequent strokes during pendulum grinding. By each grinding stroke, heat flows into the workpiece and might temper the surface zone several times before austenitization. The material model takes the cementite precipitation, the austenitization, and the martensitic transformation into account. However, the transformation of retained austenite during heating is not modeled, which could explain the overestimation of the tensile stresses in the transition region from the rehardening to the tempering zone. Furthermore, some investigations showed that the extreme short austenitization could prevent a cementite dissolution in austenite, which increases the tendency to form bainitic microstructure during cooling. This effect is being investigated for different process parameters at the same time and will be integrated in the model in the future work.

Funding Information The research project is funded by the German Research Foundation (Deutsche forschungsgemeinschaft - DFG) "Quantitative Beschreibung des Eigenspannungsverlaufs beim Tief- und Pendelschleifen von 100Cr6" (BR 1844/12-1, KL 500/122-1).

References

1. Brinksmeier E (1991) Prozess- und Werkstückqualität in der Feinbearbeitung. VDI-Verl, Düsseldorf
2. Brinksmeier E, Aurich JC, Govekar E, Heinzel C, Hoffmeister HW, Klocke F, Peters J, Rentsch R, Stephenson DJ, Uhlmann E, Weinert K, Wittmann M (2006) Advances in modeling and simulation of grinding processes. CIRP Ann 55:667–696. https://doi.org/10.1016/j.cirp.2006.10.003
3. Doman DA, Warkentin A, Bauer R (2009) Finite element modeling approaches in grinding. Int J Mach Tools Manuf 49:109–116. https://doi.org/10.1016/j.ijmachtools.2008.10.002
4. Carsten H (2009) Schleifprozesse verstehen: Zum Stand der Modellbildung und Simulation sowie unterschützender experimeteller Methoden. Habilitation, Stiftung Institut für Werkstofftechnik, Bremen
5. Zhang L, Mahdi M (1995) Applied mechanics in grinding—IV. The mechanism of grinding induced phase transformation. Int J Mach Tools Manuf 35:1397–1409. https://doi.org/10.1016/0890-6955(95)93590-3
6. Mahdi M, Zhang L (1999) Applied mechanics in grinding. Part 7: residual stresses induced by the full coupling of mechanical deformation, thermal deformation and phase transformation. Int J Mach Tools Manuf 39:1285–1298. https://doi.org/10.1016/S0890-6955(98)00094-7
7. Mahdi M, Zhang L (2000) A numerical algorithm for the full coupling of mechanical deformation, thermal deformation and phase transformation in surface grinding. Comput Mech 26:148–156. https://doi.org/10.1007/s004660000162
8. Brinksmeier E, Heinzel C, Christian B, Wilke T (2003) Simulation of the temperature distribution and metallurgical transformations in grinding by using the finite-element-method. Prod Eng 10:9–14
9. Salonitis K, Chryssolouris G (2007) Thermal analysis of grind-hardening process. Int J Manuf Technol Manag 12:72–92. https://doi.org/10.1504/IJMTM.2007.014143

10. Weiß M, Klocke F, Barth S, Rasim M, Mattfeld P (2017) Detailed analysis and description of grinding wheel topographies. J Manuf Sci Eng 139:1–9. https://doi.org/10.1115/1.4035531
11. Duscha M (2014) Beschreibung des Eigenspannungszustandes beim Pendel- und Schnellhubschleifen. Dissertation, RWTH Aachen University, Aachen.
12. Bhadeshia H, Honeycombe R (2017) Steels: microstructure and properties. Elsevier Ltd., Oxford
13. Shah A (2011) Prediction of residual stresses due to grinding with phase transformation. Dissertation, Lyon.
14. Simsir C (2014) Modeling and Simulation of Steel Heat Treatment-prediction of Microstructure, Distortion, Residual stress and Cracking. In: Dosset JL and Totten GE (eds) ASM Handbook: Steel Heat Treating Technologies, Vol. 4B. Materials Park, Ohio. https://doi.org/10.31399/as.hb.v04.a005950
15. Fischer FD, Sun WP, Tanaka K (1996) Transformation-induced plasticity (TRIP). Appl Mech Rev 49:317
16. Avrami M (1940) Kinetics of phase change. II transformation-time relations for random distribution of nuclei. J Chem Phys 8:212–224. https://doi.org/10.1063/1.1750631
17. Barmak K (2010) A commentary on: reaction kinetics in processes of nucleation and growth. Metall Mater Trans A 41:2711–2775. https://doi.org/10.1007/s11661-010-0421-1
18. Surm H, Kessler O, Hunkel M, Hoffmann F, Mayr P (2004) Modelling the ferrite/carbide → austenite transformation of hypo-eutectoid and hypereutectoid steels. J Phys IV France 120:111–119. https://doi.org/10.1051/jp4:2004120012.
19. Eser A, Broeckmann C, Simsir C (2016) Multiscale modeling of tempering of AISI H13 hot-work tool steel – part 2: coupling predicted mechanical properties with FEM simulations. Comput Mater Sci 113:292–300. https://doi.org/10.1016/j.commatsci.2015.11.024
20. Li H, Gai K, He L, Zhang C, Cui H, Li M (2016) Non-isothermal phase-transformation kinetics model for evaluating the austenitization of 55CrMo steel based on Johnson–Mehl–Avrami equation. Mater Des 92:731–741. https://doi.org/10.1016/j.matdes.2015.12.110
21. Koistinen DP, Marburger RE (1959) A general equation prescribing the extent of the austenite-martensite transformation in pure iron-carbon alloys and plain carbon steels. Acta Metall 7:59–60. https://doi.org/10.1016/0001-6160(59)90170-1
22. Leblond JB, Mottet G, Devaux JC (1986) A theoretical and numerical approach to the plastic behaviour of steels during phase transformations—II. Study of classical plasticity for ideal-plastic phases. J Mech Phys Solids 34:411–432. https://doi.org/10.1016/0022-5096(86)90010-4
23. Leblond JB, Mottet G, Devaux JC (1986) A theoretical and numerical approach to the plastic behaviour of steels during phase transformations—I. Derivation of general relations. J Mech Phys Solids. 34:411–432
24. Schmitz GJ, Engstrom A, Bernhardt R, Prahl U, Adam L, Seyfarth J, Apel M, de Saracibar CA, Korzhavyi P, Ågren J, Patzak B (2016) Software solutions for ICME. JOM 68:70–76. https://doi.org/10.1007/s11837-015-1718-8
25. Jablonka A, Harste K, Schwerdtfeger K (1991) Thermomechanical properties of iron and iron-carbon alloys: density and thermal contraction. Steel Res 62:24–33. https://doi.org/10.1002/srin.199101722
26. Acht C, Dalgic M, Frerichs F, Hunkel M, Irretier A, Lübben T, Surm H (2008) Ermittlung der Materialdaten zur Simulation des Durchhärtens von Komponenten aus 100Cr6. HTM 63:234–244. https://doi.org/10.3139/105.100470
27. Orlich J, Rosen A, Wieast P (1973) Atlas zur Wärmebehandlung der Stähle. Band 3: Zeit – Temperatur – Austenitisierung – Schaubilder. Stahleisen mbH, Düsseldorf
28. Sallem H, Hamdi H (2015) Analysis of measured and predicted residual stresses induced by finish cylindrical grinding of high speed steel with CBN wheel. Procedia CIRP 31:381–386. https://doi.org/10.1016/j.procir.2015.03.080